Journal Name

ARTICLE

A review on the laser-assisted flow deposition method: growth of ZnO micro and nanostructures

Joana Rodrigues*, António J. S. Fernandes, Teresa Monteiro, Florinda M. Costa

Zinc oxide (ZnO) is a widely versatile semiconductor with major importance from the technological point of view, presenting the advantage to be grown by a large number of techniques and with one of the richest varieties of morphologies. Due to the special interest of this semiconductor, several methods have been developed to control the production of its nanostructures. Herein, we report the development of a vapour-based method, designated by laser-assisted flow deposition (LAFD), able of producing ZnO micro and nanocrystals with different morphologies, with a high crystalline and optical quality. This new process allows high yield of ZnO production, showing great prospects for scalable applications. In the present work, we review in detail the main growth parameters and their relationship with the produced morphologies, in addition to their influence in the structural and optical properties. Furthermore, an assessment of the possible growth mechanisms that may be involved in this new method is reported. Some potential applications of the ZnO structures produced by LAFD were also evaluated, with focus on the photocatalysis and photovoltaic fields. Additionally, the possibility of synthesizing ZnO composite nanostructures, as well as the growth of other metal oxides using this technique was explored.

1. Introduction

ZnO is a wide-bandgap semiconductor ($E_g \sim 3.4$ eV at low temperature [1]) that has been extensively studied in the past decades due to its wide range of applications. It is a key technological material [1,2] and is considered one of the most versatile materials in terms of morphology. It presents one of the richest varieties of nanostructures, which are known to offer different functional behaviours. Properties like high surface-area, high crystallinity, nontoxicity, biological compatibility, and improved optical and electrical response make ZnO micro and nanostructures extremely desirable in various fields, including photovoltaic devices [3–5], gas sensors [6], photocatalysis [7], biosensors, tissue engineering, drug delivery systems and cancer diagnostics [8,9], among others. A variety of methods have been used to produce ZnO nanostructures (*e.g.* thermal evaporation, hydrothermal synthesis, colloidal synthesis, etc.), leading to very diverse shape, size and physical properties [10]. The development of growth procedures capable of tuning the micro/nanocrystals morphology and enabling the correlation between their morphologies and size-related physical properties is widely desirable for optimization in many potential applications [6,11,12]. Therefore, one of the focuses of the research community is to achieve simple and cost-effective processes for mass-scale production [6]. In the case of ZnO, several approaches have been reported to accomplish this goal [6,7,13–15]. For instance, thermal evaporation-based methods are very popular for low-cost ZnO fabrication, since a simple process is involved, not requiring expensive reagents or equipment [16]. Typically, source materials are vaporised at high temperatures and then the resultant vapour phase(s) condense(s) under certain controlled conditions (*e.g.* temperature, pressure, atmosphere and nature of the substrate) to form the desired products [17]. Several variations of these techniques have been employed for the synthesis of ZnO material with distinct morphologies.

In this paper, we report such a vapour-based method, designated by laser-assisted flow deposition (LAFD), which has been developed by our research group in the last few years. This technique exhibits a high yield of micro and nanostructures' production, with potential for scalable applications [18–22]. Some key advantages regarding the traditional methods include being catalyst-free, remotely heating by the use of a focused laser beam and the reduced presence of undesired contaminations, since neither crucibles nor additional reagents/solvents besides the materials' precursors are needed.

This method derives from the laser floating zone technique [23–25] and takes advantage of the growth apparatus constructed for such application, namely the CO_2 infrared laser as heating source and the reflective set-up to direct the laser beam to the precursor material. In LAFD, typically solid (usually powders) sources are vaporised at elevated temperatures and then the resultant vapour phases condense under specific controlled conditions (*i.e.* temperature, pressure or atmosphere) to form the desired products. To enable this technique, it is necessary that the laser heating vaporises the precursor material instead of melting it, supported by the proximity of the melting and ebullition temperatures and high temperature gradient inside the growth chamber, or by thermal decomposition at temperatures lower than the melting point (at ambient pressure). Therefore, only materials that fill these requirements can be grown by LAFD. Up to now, our group have successfully grown both ZnO[5,18,19,21,22,26] and tin oxide (SnO_2)[20] micro and nanostructures. Moreover, by incorporating additional compounds into the

Departamento de Física & I3N, Universidade de Aveiro, Campus Universitário de Santiago, 3810-193 Aveiro, Portugal
* Email corresponding author: joana.catarina@ua.pt

precursors, it is possible to achieve the formation of intentionally doped materials [20], as well as composites structures [21] in a single growth step, avoiding additional and time-consuming procedures. Particularly, one of the advantages of this technique resides in the possibility of *in-situ* production of the semiconductor's nanostructures onto other materials, preserving their structure and alignment, as the case of vertically aligned carbon nanotubes (CNTs), where this method proved to avoid the collapse of the aligned CNT structures [22].

The main focus of the LAFD development has been given to the ZnO crystals, since the structures produced by this method[5,18,19,21,22,26] already revealed high structural and optical quality. In fact, these structures proved to be of special interest for several applications, which includes photocatalysis[27] and the production of photovoltaic cells [5]. Therefore, herein we highlight the fundamental principles of operation of LAFD and review in detail the main growth parameters and their relationship with the produced ZnO morphologies, in addition to their influence in the structural and optical properties. Furthermore, the production of other metal oxides using this technique is also mentioned.

2. LAFD technique: experimental description

Figure 1 depicts a schematic representation of the LAFD process and the main components of the growth system. The apparatus is comprised by a CO_2 laser (λ= 10.6 μm, maximum power of 200 W) as heating source, coupled to a reflective optical set-up that produces a circular crown-shaped laser incidence. As such, the laser beam is directed from the parabolic mirror to the tip of the precursor, hitting the source of material all around its surface, with a tilted direction. It is worth to mention that all the mirrors that comprise this optical set-up are coated with a gold layer, avoiding degradation by the infrared laser irradiation and assuring their long-term stability.

This highly-focused laser incidence causes the local heating of the precursor, leading to the thermal decomposition of the material's source when high enough temperatures are attained to promote this process. For instance, in the case of ZnO, which has a high melting point ($T_m \sim 1977$ °C), its thermal decomposition rapidly starts at temperatures above ~ 1376 °C [28]. After the formation of the vapours containing the precursor's materials needed for the growth of the crystalline structures, convection transports the generated gases to the upper regions kept at lower temperature, where a sample holder is placed attached to the upper spindle of the system. Substrates can be used to collect the formed products or the as-produced material can be directly deposited on the holder. As the material evaporates, the system is automatically fed by moving the precursor rod, at a controlled speed (translation motor), to the laser focusing zone, thereby ensuring a continuous production process. The motors near the planar and the parabolic mirrors are responsible for the translational and rotational movements of the feed rod precursor and the sample holder, respectively.

Typically, the used precursors are shaped into cylindrical rods (by mixing commercial powders with a ligand (PVA – alcohol polyvinyl) to keep the powders aggregated) in order to be attached to the lower spindle of the system. To improve the homogeneity of the deposition, it is important to assure a proper alignment between the precursor and the centre of the holder, as well as to keep them under rotation during the growth process.

The temperature reached inside the growth chamber is controlled by the applied laser power and constitutes one of the key parameters that will influence the growth process. Figure 2a shows the correspondence between the applied power and the attained temperature (considering a distance of 7 mm between the top of the precursor and the surface of the holder).

Additionally, the growth atmosphere can also be controlled by evacuating the growth chamber and adding the desired gas (or combination of gases). Pressures up to 2 atm can be supported by the growth apparatus.

In general, the main parameters that can be controlled with this technique are: laser power (*i.e.* temperature), feed rate, precursor rotation and atmosphere inside the chamber.

3. LAFD applied to ZnO growth

In the case of ZnO, different morphologies can be obtained by LAFD as a result of different kinetic/thermodynamic (*e.g.* temperature, pressure and oxygen content) local conditions verified in different regions of the chamber [18,19]. Three types revealed to be dominant: nanoparticles (NPs), tetrapods (TPs) and microrods (MRs) (scanning electron microscopy (SEM) images shown in Figure 2 b to d).

The growth of the crystal is determined by the combination of external conditions, such as temperature, supersaturation, reaction time or additives, and structural related factors, like surface energy, anisotropy, intermolecular bonds or dislocations [7,16,29,30]. There are three basic steps involved in the formation of a crystal from an initially disordered phase: supersaturation of the liquid or gas phase, nucleation and growth of the nuclei into a crystal [16]. When the growth of the crystal starts (from a supersaturated vapour phase), the material tends to condensate and form small nuclei that continuously attach material until it develops as a seed for the formation of the crystal. As time passes, as long as the external conditions are kept favourable, the growth process starts to be conducted by the surface energy of the formed faces of the crystal [31]. Macroscopically, a crystal has different kinetic parameters for different crystal planes, which can be potentiated under controlled growth conditions. Thus, after the initial period of nucleation, a crystallite will commonly develop into a three-dimensional object with well-defined low index crystallographic faces [17].

The shape of the crystal is governed by the relative difference on growth rates at various faces of the crystal [30]. The growing surface would assume the shape for which the surface energy is the lowest [16]. Therefore, in general, the surface area of a crystal decreases with increasing surface energy and higher growth rates. The planes with higher growth rates and surface energy tend to disappear first, and consequently the planes with slower growth rates and lower energy dominate the morphology of the crystal [7,30–32]

Journal Name

ARTICLE
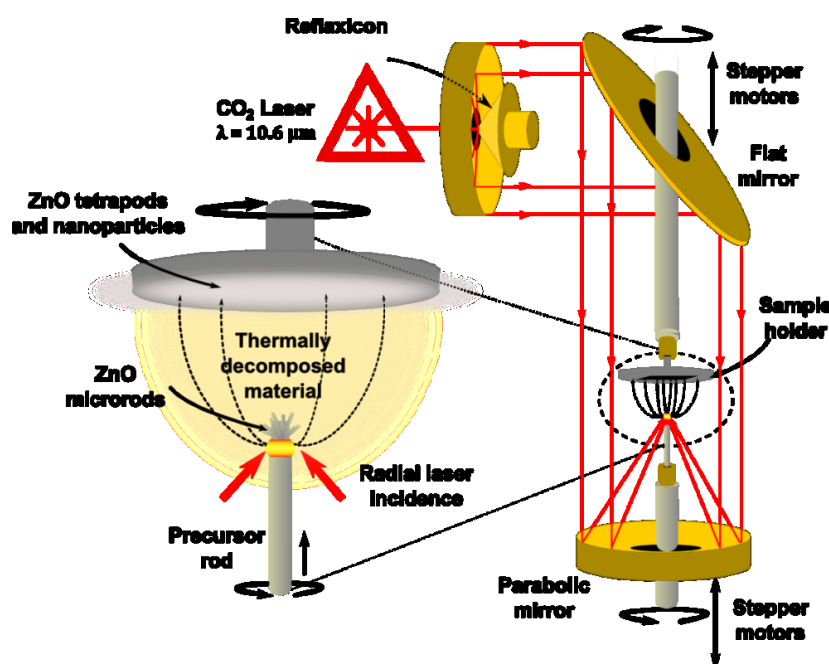
Figure 1 – Schematic representation of the LAFD process and growth apparatus. The inset corresponds to a close-up of the growth region with the laser incidence area being clearly shown and indicated by the red arrows.

The bonds in the structure also play a significant role in crystal shape. The crystals tend to elongate into the direction of the strongest bonds [31]. Since the interaction among the charges is governed by their distribution, the crystalline structure is arranged in order to minimize the Coulomb energy and usually the polar surfaces possess the highest surface energy [32]. In the case of wurtzite (WZ) ZnO, the structure is described as a stacking of alternating planes comprised by tetrahedrally coordinated Zn^{2+} and O^{2-} along the *c*-axis. This anisotropic structure leads to differences in the surface energy of the faces of the crystal and a strong anisotropy in their growth rate [7,33]. This is the main reason why ZnO exhibits a wide range of morphologies. Therefore, an appropriate choice of growth conditions allows to control the kinetic parameters for the different planes of the crystal, tuning the growth rates along the different faces [17].

In the case of the LAFD, the growth parameters that proved crucial for the formation of the different ZnO morphologies are: laser power (temperature) and atmosphere. Even though other parameters were tested, namely distance between the precursor and the substrate, growth time and feeding speed, these were found to have limited influence in the produced structures.

It was observed that the growth of crystals with dimensions on the micrometric scale (MRs) is promoted in the high-temperature regions, close to the precursor tip, where there is permanent air convection. These crystals exhibit a high aspect ratio and present lengths of several micrometres and diameters in the order of hundreds of nanometres. The nanoscale structures (NPs and TPs) are formed in the holder region, where the temperature is lower. Depending on the applied laser powers, only NPs (laser power around 20-22 W) can be produced, or a combination of both, with the TPs morphology dominating as the power increases (>25 W). A first layer of NPs is always present, as it corresponds to the initial heating stage of the process. Thus, MRs and TPs/NPs are frequently produced at the same run of growth, although in different regions of the growth chamber and depending on the growth parameters. Table 1 depicts a summary of the main LAFD growth conditions that result in the formation of the different ZnO morphologies.

3.1. Tetrapods and nanoparticles.

Proposed growth mechanisms Figure 3 shows SEM images of the ZnO structures grown near the substrate surface, summarizing the results obtained using several combinations of laser power and growth atmosphere. The distance between the precursor rod and the holder was kept for all the applied conditions (7 mm), as well as the growth time (3 min). These samples were grown in silicon, sapphire, glass and aluminium substrates, with no significant differences found in the formed nanostructures for the different substrates. This observation led to the assumption that both the NPs

and TPs are grown in the vapour phase and are unaffected by the nature of the substrate used to collect the as-grown material. It is also worth to mention that, besides air and N$_2$ atmosphere, which results are shown in Figure 3, an argon atmosphere was also used, leading to similar outcomes (at the same pressure). For this reason, only the samples produced under air and nitrogen atmosphere are discussed herein. It was observed that the oxygen availability and/or the oxygen pressure inside the chamber was the parameter that ruled the growth, instead of the nature of the growth atmosphere. In fact, as will be discussed later, the amount of oxygen available to react with zinc was seen to be of paramount importance.

Starting the analysis by considering the structures grown in air (first column of Figure 3), one clearly sees that by gradually increasing the laser power from 20 to 35 W dramatic changes arise. It is important to note that below 20 W no deposition was seen to occur.
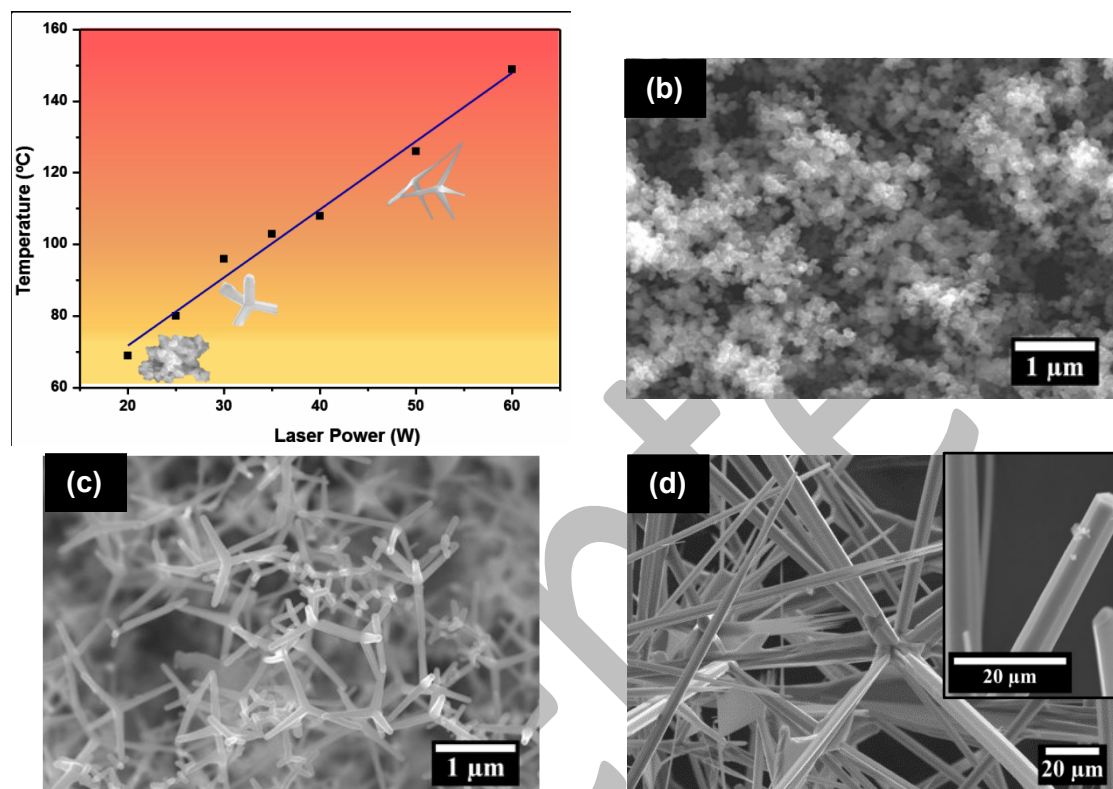
Figure 2 – (a) Temperature at the surface of the holder as a function of laser power, showing examples of ZnO morphologies that are formed at the different temperature ranges. SEM micrographs of the three main morphologies produced by LAFD: (b) NPs, (c) TPs and (d) MRs.

Table 1 – Summary of the dominant morphologies obtained under different combinations of laser power and growth atmosphere. For the TPs, the values shown correspond to the length of the branches. For the MRs, the L stands for length while D indicates diameter.

Laser power (W)	Air atmosphere		Oxygen-poor atmosphere		Region of the chamber
	Morphology	*Dimensions*	*Morphology*	*Dimensions*	
20	NPs	~ 100 nm	NPs	~ 100 nm	Sample holder
25	TPs	~ 100 nm	NPs	~ 100 nm	
30	TPs	~ 500 nm	NPs	~ 100 nm	
> 35	TPs	~ 1 μm	TPs	~ 500 nm	
> 30	MRs	L ~ tens of μm D ~ 200-500 nm to a few μm	MRs	L ~ tens of μm D ~ 100-500 nm to a few μm	Tip of the precursor

Journal Name

ARTICLE

Above this threshold (20 W), NPs can be produced and constitute the only morphology obtained. Generally, these NPs present a polyhedral configuration with an average size around 100 nm, even though smaller particles can be found. In most cases, the particles appear agglomerated and slightly coalesced. Typically, only a very thin layer of these structures is deposited on the surface of the substrate and was found to be fairly attached to it, independently of the its nature. Increasing the laser power from 20 W to 25 W resulted in the formation of small TPs with cylindrical/prismatic-like branches, exhibiting average lengths lower than 100 nm. These structures display a tetrahedral shape with four branches extended from a central part. With further increasing in the applied laser power (up to 30 W), the branches of the TPs become longer and a decrease of the thickness along the branch starts to occur. Higher powers lead to wider TPs, with long branches and sharper tips, as seen in Figure 4 for the samples grown with 35 W (in air). At this power (and higher), most of the branches of the TPs exhibit a needle-like shape, showing similar morphology and dimensions within the same TP. Increasing the power beyond 35 W results in the production of larger size TPs. However, the most important change does not correspond to the dimensions of the TPs but their size distribution. Dimensions from hundreds of nanometres to a few micrometres were measured in the same run of growth for such high powers. This can be associated with the different local kinetic conditions inside the chamber. Low temperatures limit the TPs growth, thus a sample with more uniform TPs' sizes is produced. When the power/temperature is increased, a higher temperature gradient is present inside the chamber, resulting in significant differences on the thermodynamic and kinetic conditions in the different regions and, consequently, in more distinct TPs' sizes.

Besides the effects in the shape of the TPs, it was also observed that high powers result in a high TPs/NPs ratio. Nevertheless, as mentioned previously, even in this case a first layer of NPs is deposited. Such nanocrystals are always present, forming an interconnected network of NPs and TPs, whose TPs/NPs ratio depends on the applied laser power (heating). Such network can be advantageous for several applications, as in the case of the fabrication of photovoltaic cells that will be discussed later on.

The TPs' morphology is very common for ZnO and the formation of such structures have been widely studied by different researchers [34–39] with the aim of clarifying their growth mechanisms, with the most accepted models being the ones of Shiojiri *et al*. [35] and Iwanaga *et al.* [36,37]. In the first, the authors assume that the core from where the nucleation takes place corresponds to octahedral nanocrystals of zinc blend structure with four {111} facets of zinc and other four of oxygen. Afterwards, WZ ZnO crystals grow faster along the normal directions to the zinc surfaces, resulting in a TP morphology [35]. Iwanaga *et al.* [36,37] presented the so-called "octa-twin model", in which the process begins by the formation of an octahedral multiple

twin nuclei. During the growth, some of the twin-boundaries crack to release a large misfit strain and the crack openings are filled by ZnO during further growth of the particles. Then, branches grow preferentially oriented in a direction perpendicular to the (0001) surfaces. Thus, a tetrapod-shaped particle is formed with the inter-branch angles deviating from the regular tetrahedral relation due to the cracking of the octa-twin nucleus [37]. This model is accepted by many authors since it correctly describes the crystal geometry, however, up to now, none of the experiments showed that the centre core indeed contains an octahedral seed crystal [39].

Considering what was observed in the case of the structures produced by the LAFD method, the growth model proposed by Ronning *et al.* [39] seems to be the one that provides the best explanation for the formation of both NPs and TPs, depending on the applied growth conditions. This model suggests that the growth comprises a first step with the formation of small spherical ZnO clusters. Then, further condensation of Zn and O atoms leads to instability in the clusters, causing their collapse into polyhedral-shaped crystals, which include four ZnO grains, that develop into the four branches due to the faster growth rate along the *c*-axis direction of each crystal. The dimensions and the shape of the particles are seen to be dependent on the growth conditions (especially temperature), as observed in the here reported method. These may explain why, in the case of LAFD, only NPs are formed for low powers (low temperatures) and always constitute the first layer of the deposited material, which transforms into microcrystalline TPs on the top layers. This first step occurs during the initial heating stage when the laser power starts to be applied.

The exposed faces of the NPs depend on the energy of each surface [29] and the interface of the grain boundaries. If the reaction is stopped at low temperatures, the NP morphology is kept. Further heating results in the TP formation, with the growth proceeding through the most favourable crystallographic directions. This mechanism is further corroborated by the presence of a twin relation between the TP branches, as evidenced by transmission electron microscopy (TEM) analysis (not shown).

These measurements revealed that the four branches of the TPs correspond to single crystals (corroborated by electron diffraction). The interfaces between the neighbouring crystalline domains are fairly sharp, straight and connected with little lattice distortion. Chen *et al.* [40] also reported a similar growth theory that fits our observations: after decomposition of the ZnO precursor into Zn (or Zn suboxides (ZnO_x, x<1) [41]) and oxygen vapours generated at the high temperature material's source region, both elements (or compounds) are then transported to the lower temperature regions, above the laser incidence spot. At this stage, part of the Zn reacts with the oxygen and the nucleation process starts to form the nuclei, leading to the formation of small ZnO particles. These particles can act as nucleating seeds for the TP growth. Owning to their polyhedral

shape with WZ structure, the four branches of TPs can thus grow further out from the nucleus crystal simultaneously via a vapour-solid (VS) mechanism. The growth is fed by a continuous condensation and diffusion of Zn and oxygen, provided that the conditions are favourable for the process to carry on [40].

As stated before, the polar surfaces have the highest surface energies for the WZ ZnO and thus, a morphology that tends to supress these surfaces is favourable. The TP shape is the most energetically favourable since it offers the minimum energy ratio between interface and surface areas of the crystals. The shape and length of the TPs' branches are mainly governed by the growth conditions, particularly the Zn and O vapour pressures, as well as by the anisotropy between the growth rate of each direction and the surface energy, which are temperature-dependent [6,39]. If the growth rate along the *c*-axis is considerably larger than on $(11\bar{2}1)$ surfaces, the branches of the TPs will exhibit a high aspect ratio. Alternatively, if the growth rates are similar, the TPs will have a bulkier structure [39].

Qiu and Yang [42] found that, for a constant oxygen content, the size of the TPs is strongly dependent on the local temperature and Zn vapour pressure.
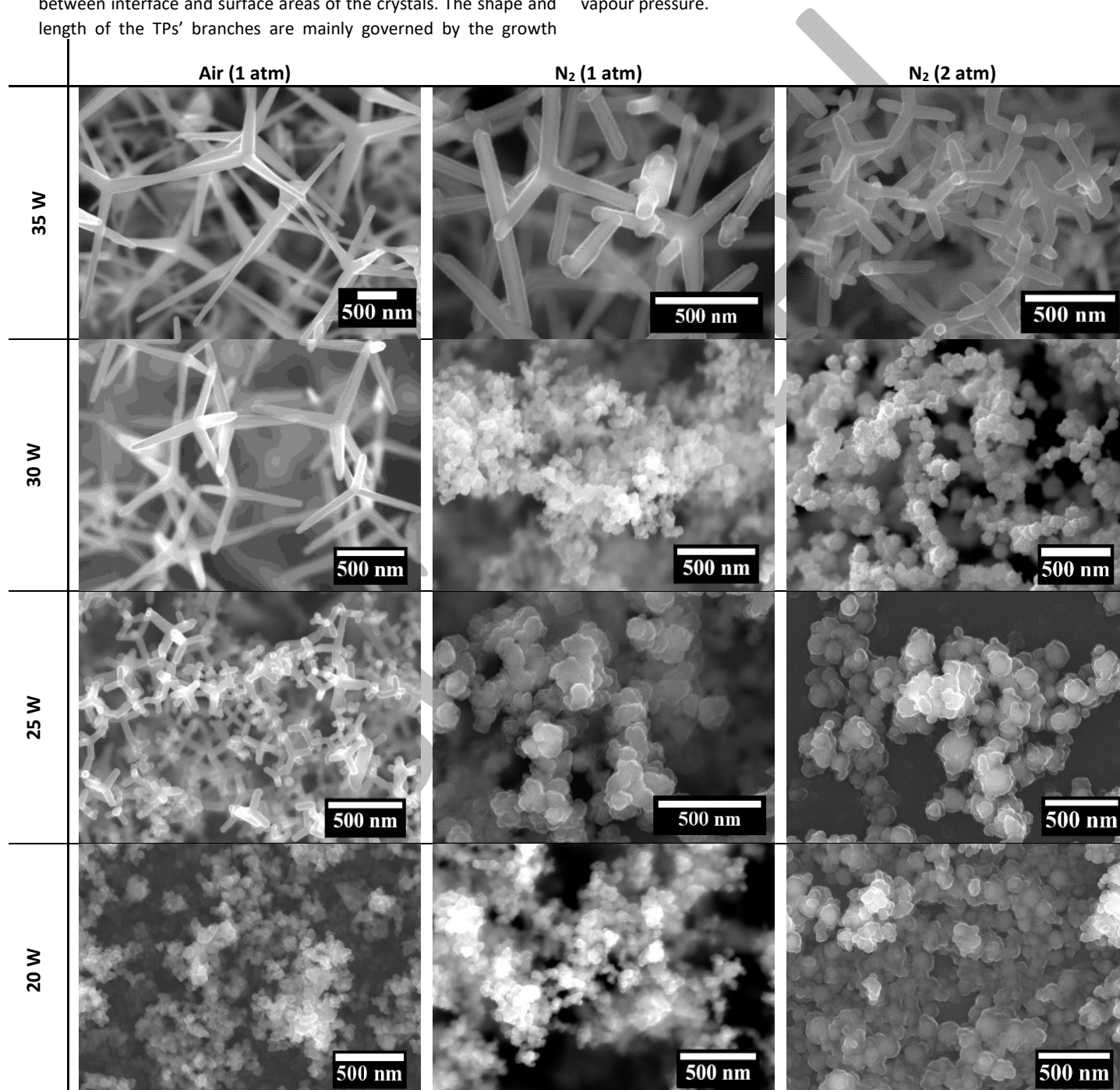
Figure 3 – SEM micrographs of the ZnO structures grown by LAFD at the lower temperature region (at the holder/substrate surface), using different laser powers and growth atmospheres.

Journal Name

ARTICLE

High temperature and high Zn vapour pressure (which is promoted by the high temperature) lead to a rapid growth into large TPs, whereas the opposite results in a slow nucleation/growth rate. The TPs formed in higher temperature regions are rapidly transported to lower temperature zones by the flowing stream, slowing down the growth rate and inhibiting the process [42]. Adjusting the temperature inside the growth chamber changes the vapour pressure. Thus, if the vapour concentration was kept at a certain value, the growth would proceed in a thermodynamic equilibrium state. In this case, the continuously incoming zinc atoms can combine with oxygen into ZnO along the [0001] direction due to its lowest surface energy, which leads to TPs' branches with almost homogeneous hexagonal pillar shape, like those observed in the samples produced at 25 W (Figure 3) [41]. However, during the growth process, the vapours' ratio (Zn/O) will be different since the amount of Zn is limited by the precursor material while oxygen is abundantly present in air. Due to this difference, the equilibrium will be broken, leading to modifications in the growth kinetics of the branches [6,41]. This low Zn vapour pressure accelerates the growth along the [0001] direction while supressing it in any other directions, sharpening the TPs' branches in a needle-like shape as the growth proceeds [6,41], in line with what is observed for higher laser powers.

It was also observed that changing the growth conditions from open air to a poor oxygen atmosphere led to significant changes in the produced morphologies. While, for the samples grown in air, TPs start to form around 25 W, under N_2 atmosphere (1 atm) this morphology only appeared for powers ≥ 35 W, presenting size and shape similar to the TPs grown with 30 W in air. For samples grown under 2 atm of N_2 pressure, a reduction of the TPs size using the same laser powers was identified (3rd column in Figure 3).

Moreover, it was noted that the produced NPs appear to have a higher degree of coalescence, forming larger agglomerated structures, likely to be due to the higher pressure inside the growth chamber. So, reducing the amount of oxygen inside the chamber leads to a decrease in the growth rate of the crystals, allowing the production of NPs up to higher laser powers, therefore, increasing the yield of the production of this morphology. Since in these controlled atmospheres the only oxygen available to react with the Zn vapour comes from the precursor (plus some residual amount that may still be present inside the growth chamber), the growth rate of the ZnO crystals will be significantly reduced, resulting in crystals with smaller dimensions. This important role of the oxygen concentration in the TPs' growth was also reported by Qiu and Yang [42]. These authors witnessed that for low oxygen concentration (< 7.5 %) most of the products obtained did not present the TP's shape. This shape only appeared when the concentration of oxygen became the dominant one. Additionally, Yan *et al.* [43] reported that, at low oxygen partial pressure, the growth of ZnO crystals is slow, experiencing a thermodynamic equilibrium during the growth process (since the only oxygen is provided from the precursors), which results in regular-shaped arms with hexagonal cross-section, as those obtained for 35 W under N_2 atmosphere (Figure 3).

Heat treatments. The influence of heat treatments in the morphology of the samples was also evaluated. Figure 4 depicts a comparison between the SEM images of a sample grown in air with an applied laser power of 20 W before (a) and after (b) the thermal annealing in air. It was observed that after being placed in an oven for 2 h at 500 °C and at atmospheric pressure (Figure 4b), though some NPs remained, most of them underwent a morphology transformation into TPs. The shape of these TPs is similar to the one obtained for the samples grown at 25 W, with bulkier branches and branch lengths around 100 nm. Thus, one can assume that the NPs produced with low laser power correspond to the nuclei from where the TPs' growth proceeds. Subjecting the NPs to a higher temperature allows the growth to carry on, forming TPs structures with an analogous shape to the ones produced directly during the LAFD process at powers higher than 25 W. The TPs grown with 25 W (air) were also subjected to thermal annealing with three different temperatures (500 °C, 600 °C and 700 °C), during 2 h (Figure 4c to f). It was found that the size of the TPs progressively increased with increasing temperature, with the branches acquiring a needle-like shape, more pronounced for higher temperatures. It is also interesting to note that in this case, where a more uniform heating was applied, the TPs' size distribution seems more homogeneous than in the case of the samples directly grown by LAFD.

3.2. Microrods

In the case of the MRs, as stated before, the growth takes place on top of the precursor rod, which simultaneously acts as the substrate for the MRs growth, as the formed crystals remain attached to it (inset in Figure 1). In this case, no significant changes were found regarding the physical properties of the crystals for the different laser powers applied during their growth. Even the size distribution of the rods seems to be similar. Although large crystals are often produced, their dimensions are mostly at the micrometre scale. Figure 2d shows a representative SEM image of the produced ZnO MRs with an applied power of 40 W. As stated before, the MRs exhibit a high aspect ratio, with a hexagonal cross-section, and are randomly oriented. The growth of structures with higher dimensions than the ones identified in the holder region is favoured both by the higher temperature verified near the laser incidence region and the higher concentration of reactant species, since the rods grow at the source of the material. Moreover, a different growth mechanism than the typical VS one accounted for the TPs and NPs is proposed to explain the significant differences observed in the dimensions and morphology of the MRs. The formation of crystals with rod morphology is proposed to be related with a vapour-liquid-solid

(VLS) process. In the conventional VLS growth, a metal droplet is usually placed on the growth front and acts as a catalysts for the growth of the crystals [44,45]. Even though such an external catalyst is not present in the LAFD growth, the formation of the MRs is likely to be promoted by a self-catalysed growth, where some liquid droplets are involved. At the laser incidence region, where high temperatures are present, both melting and evaporation of ZnO should occur almost simultaneously. The triple point of ZnO is at ~ 1977 °C under the total (Zn and O_2) vapour pressure of 1.06 atm [28]. To maintain the ZnO melt stable, the total pressure of oxygen-containing atmosphere in the growth chamber must be high (considerably larger than 1.06 atm), as well as the temperature [28]. Thus, these conditions should be met locally at the laser incidence region, where oxygen both from the precursor and atmosphere contributes largely for the total oxygen pressure. This local combination of high vapour pressure and high temperature is likely to lead to the formation of the liquid droplets. Moreover, the presence of carbon in the precursor rod (from the PVA binder) may act as reduction agent during the formation of ZnO crystals [46,47].
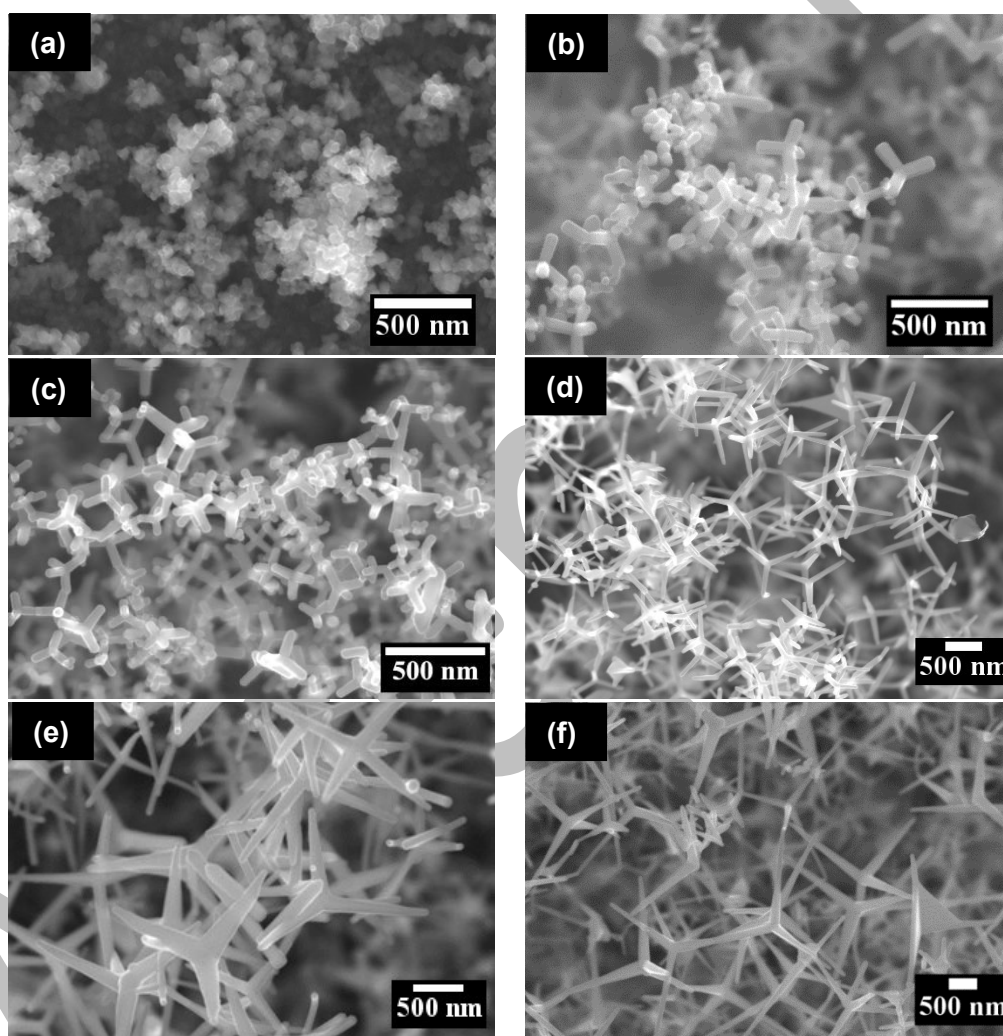
Figure 4 – SEM images of ZnO samples grown in air (a) with a laser power of 20 W and (b) subjected to a thermal annealed in air at 500 °C during 2 h. SEM images of ZnO TPs produced in air at 25 W (c) as-grown and thermal annealed in air at (d) 500 °C, (e) 600 °C and (f) 700 °C.

In fact, part of the ZnO powder can be reduced into zinc or its sub-oxides (ZnO_x) with low melting point (melting temperatures of Zn and ZnO_x (x<1) around 420 °C [45,48]), promoting the local formation of Zn/ZnO_x micro-droplets at the surface of the precursor rod. According to Xu *et al.* [46], the presence of carbon in the precursor material strongly influences the growth speed and the resultant yield, enabling the melting of ZnO, which cannot be accomplished without this element. Then, the small Zn droplets may agglomerate and fused to form larger droplets from where the ZnO MRs grow, as reported in other synthesis methods [49] (see a schematic representation in Figure 5).

Therefore, zinc and its sub-oxides not only play the role of reactants (as seen in the case of the formation of the TPs and NPs in the low temperature region) but also act as energetically favoured sites for adsorption of oxygen [46]. These may explain why some of the MRs are attached to each other (see Figure 2d), as well as to the precursor rod (see SEM image 4 in Figure 6). Figure 6 shows a longitudinal-section image of the tip of the precursor after the growth and removal of the MRs. Three distinct regions can be clearly identified, corresponding to different stages of the growth process. The first region (labelled 1 in Figure 6) corresponds to the top of the precursor which was subjected to the laser incidence and where the MRs were

formed and afterwards detached. This is the region from where ZnO evaporates to feed the growth of the different micro and nanocrystals, resulting in a partial consumption of the material. A porous and granular structure can be observed, exhibiting well-defined grains with polyhedral shape (SEM image 1). This considerably differs from the third region (labelled 3 in Figure 6) where the precursor material was not heated by the laser. This last region is seen to be constituted by a mixture of the ZnO commercial powders and the PVA binder, resulting in a porous structure, however without evidencing any polyhedral crystals, as in the previous case, most likely due to the presence of the amorphous PVA.

As the growth proceeds, the part of the precursor that is being heated and pulled upwards remains at a high temperature region, which can be viewed as a kind of thermal treatment, leading to the formation of the polyhedral microparticles that are observed in region 1 of Figure 6. On the other hand, the intermediate region (labelled 2 in Figure 6) appears to be denser than the remaining ones, as would be expected if a densification from melting is considered. This region coincides with the spot where the laser was focused before being turned off.
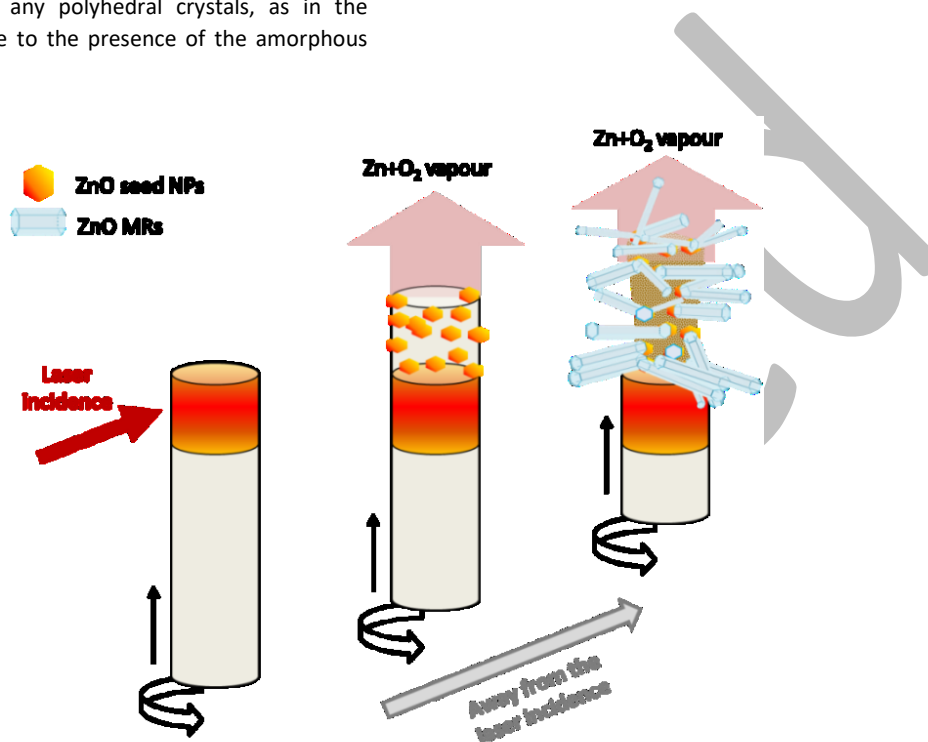

Figure 5 – Schematic representation of the MRs growth process.

Therefore, a fast cooling of the material took place, not giving enough time for the rearrangement of its structure and grain formation. This puts in evidence our assumption that melted material was likely to be present at some point of the heating/growth process, which is also corroborated by image 4 in Figure 6, where part of the precursor with as-grown MRs attached to it can be clearly identified. During the mechanical detachment of the MRs from the precursor rod, part of the microparticles that now constitutes the heated precursor remained attached to the as-grown MRs, showing the interface between both structures. Some of these microparticles seem to have some degree of coalescence, suggesting the possibility of the presence of a liquid phase as the starting point for the MRs nucleation.

Taking into account the considerations made above, we proposed that, during the LAFD process, the freshly-formed reactant gases resultant from the thermal decomposition of part of the precursor, as well as from the oxygen in the atmosphere, attain supersaturation and cause the precipitation of the material, leading to the formation of both the nanoscale structures at the holder region (TPs and NPs) by the VS mechanism, and feeding the growth of MRs at the precursor tip by VLS. In the case of the MRs, as the reactant

concentration increases, the ZnO nuclei formed by the ZnO_x droplets at the surface of the precursor are fed by the surrounding gases and grow in such a way that leads to the reduction of the strain energy and the formation of low energy facets to attain the rod morphology [44,50].

The diameter of the rods should be related to the size of the droplets from where the nucleation takes place [51]. As the precursor moves upwards, moving the newly grown MRs away from the laser incidence (Figure 5), a new precursor surface is exposed to the heating source, continuously offering new nucleation sites along with fresh precursor reactants. Moreover, as the heating proceeds, branched structures start to form, likely due to the formation of Zn droplets on the surface of the primary MRs. It is well-known that the droplets can be formed in a supersaturated system as a stable nucleus, playing the role of both reactant and catalyst [48,52]. Further adsorption of material at the surface of these droplets leads to the formation of ZnO crystalline particles, which then diffuse and migrate to suitable lattice sites, undergoing a nucleation and growing process [52]. As discussed in the case of the TPs' formation, when the supersaturation decreases to a stable status, an equilibrium condition is approximately achieved, likely favoured by the higher

concentration of reactant species, when compared to the holder region. Such condition tend to favour the formation of regular-shaped hexagonal cylinder structures, as evidenced in Figure 7 [52].

These rod structures are one of the most common morphologies of ZnO. Due to the chemically active polar surfaces with electrostatic charges, the rods with the WZ structure frequently show a hexagonal morphology oriented along the polar growth direction, in order to minimize the total surface energy and giving rise to a uniaxial polarization along the *c*-axis [7,29].

According to the periodic bond chain (PBC) theory, the velocities of the ZnO crystal growth in different directions are: $v_{<0110>} > v_{<0111>} > v_{<0001>}$ [30,31].
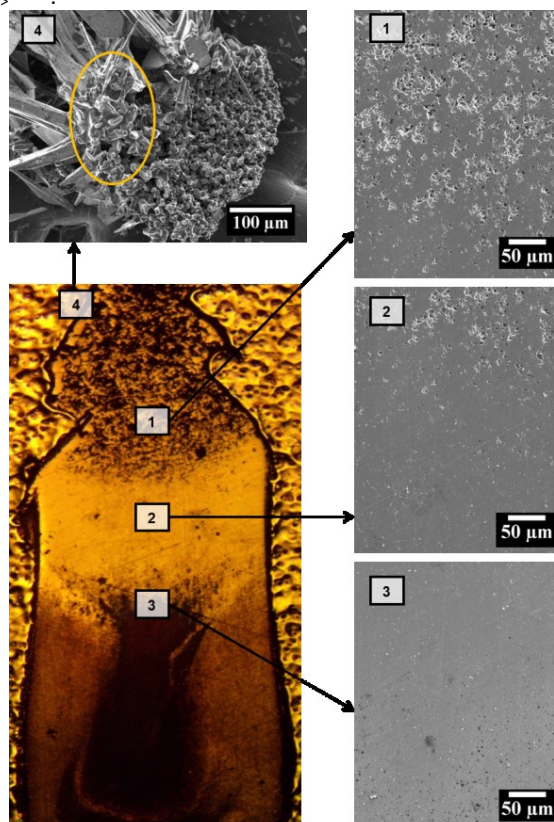

Figure 6 – Longitudinal-section image of the tip of the precursor rod (diameter ~ 2 mm) showing three distinct regions: (1) region subjected to laser incidence, from where ZnO decomposition takes place to feed the growth process of the micro and nanocrystals. This is also the region where the MRs are formed and attached. (2) Intermediate region exposed to the laser prior to the shutter activation; and (3) interface between region 2 and the precursor rod not subjected to the laser beam. Region 4 corresponds to the interface between the precursor rod and the formed MRs. The SEM micrograph shows part of the precursor particles attached to the as-grown MRs.

Moreover, as reported by several authors [29,53], the fact that the energy of the polar (000$\bar{1}$) plane is much larger than that of the non-polar ones leads to a polar growth direction with equivalent non-polar side facets with hexagonal symmetry, which are low-index crystallographic planes and low-energy surfaces [29]. Indeed, in the case of the LAFD MRs, the highest growth rate was observed along the *c*-axis, with the extremities of the rod being composed by the

polar (0001) and (000$\bar{1}$) planes and the large lateral facets corresponding to the nonpolar {01$\bar{1}$0} and {2$\bar{1}$$\bar{1}$0} family of planes, which have lower surface energy (Figure 7).

A significant number of MRs was analysed by electronic microscopy techniques. The analyses showed that most of the lengths of the probed MRs are in the range of several μm with diameters ranging from 200 - 500 nm to a few μm. Moreover, a homogenous composition was found along the growth and radial directions. HRTEM analysis and the corresponding Fast Fourier Transform (FFT) confirmed that the majority of the studied MRs grew along the [0001] direction. No dislocations or basal stacking faults perpendicular to the general [0001] growth direction were found for the entire length of the analysed MRs. Moreover, the lateral walls of the MRs appear almost atomically flat without roughness or a shell structure. Details regarding the TEM analysis of the MRs can be found in reference [26].
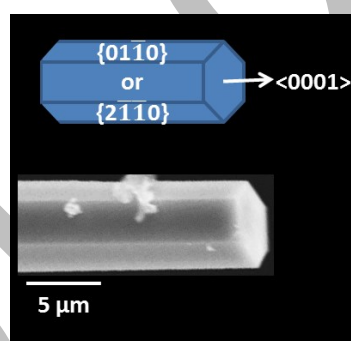
Figure 7 – Typical morphology of the LAFD-produced ZnO MRs and the schematic representation of the corresponding facets. The indexation was made in accordance with the TEM results and reference [17].

Under an oxygen-poor atmosphere the production of MRs is strongly hampered, leading to the formation of fewer crystals (considering the same laser power). Thus, the study of the samples grown in this type of atmosphere was mainly focused on the material deposited (NPs and TPs) on the substrate/holder. Nevertheless, the crystallinity of the MRs grown under an N$_2$ atmosphere (2 atm) was also evaluated by TEM (see sub section 4.1 below), revealing that the dimensions and crystalline quality of the MRs produced in such conditions were similar to those grown in air. This leads to the conclusion that growing in an oxygen-poor atmosphere does not seem to significantly affect the crystallinity of the LAFD-produced MRs, only its production rate.

4. Characterization of the LAFD-produced ZnO structures

4.1. Structural properties

The structural properties of the LAFD structures were further analysed by TEM and XRD measurements. All the planes depicted in the diffraction patterns can be associated to the WZ crystalline structure for all the morphologies [19] (see examples of XRD patterns obtained for TPs in Figure 8) and confirming the high crystallinity of the LAFD-produced samples, independently of the growth conditions, as supported by the narrow full width at half maximum (FWHM) values of the diffraction maxima. Moreover, the position of

the diffraction peaks was seen to be fairly constant regardless the applied power and even the growth atmosphere. Lattice parameters of a $(b) \sim 3.24$ Å and $c \sim 5.22$ Å were found for the TPs' structures, in line with the values reported for the bulk material [54,55]. In the case of the MRs, lattice constants of $a = b = 3.25$ Å and $c = 5.21$ Å were determined, as well as the angles of the WZ structure, $\alpha = \beta = 90^o$ and $\gamma = 120^o$ [18,19].

HRTEM analysis on the TPs structures corroborated their excellent crystalline quality and the absence of dislocations or stacking faults along the entire nanostructure, even when high laser powers are used (Figure 9, TPs grown at 60 W).
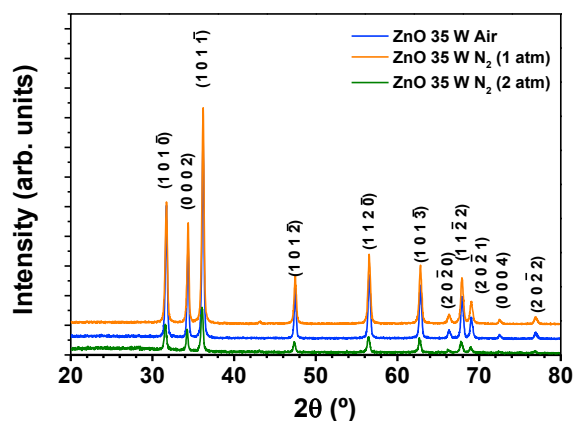

Figure 8 – XRD patterns of the TPs grown at 35 W with different atmospheres. The spectra are vertically shifted for clarity.

In fact, increasing the laser power does not seem to significantly influence the crystallinity of the produced material. Taking into account the orientation of the TP branch in the HRTEM image, it was concluded that the [1$\bar{1}$01] was the crystallographic direction of the growth for this specific TP branch. However, analysis in different branches of different TPs revealed other growth directions, namely the typical c-direction [0001], which seems to be the dominant one [18]. In fact, Figure 9c shows a HRTEM image acquired in a TP branch grown along the [0001] direction, depicting an estimation of its interplanar spacing (5.24 Å). The differences found in the growth direction of the branches may be related to the different faces exposed in the nuclei particles from which the TP growth proceeds. It was seen that the NPs exhibit irregular shapes that differ from particle to particle, evidencing the presence of distinct surface faces. Considering the NPs/TPs samples grown under N_2 atmosphere and at higher pressure (2 atm), using a laser power of 35 W, TEM results (Figure 10) showed that, in line with the SEM analysis, under such conditions the TPs growth is reduced, leading to a decrease in their amount and size, while a larger number of NPs is obtained. The NPs' quantity is comparable to that found for the TPs (Figure 10a), which strongly contrasts with the samples grown in air at the same laser power. The shape and dimensions of the produced TPs can be well seen in Figure 10b. In this case, the branches do not exhibit the needle-like shape characteristic of the TPs grown in air, presenting bulkier branches instead.

The NPs are represented in Figure 10c, showing a wide size distribution. From this TEM image, the polyhedral shape of the NPs is unambiguously identified, though with a number of different

shapes. The HRTEM study, together with the FFT analysis (Figure 10d), proved that the crystalline quality of the crystals is kept even under a low-oxygen atmosphere. No crystalline defects or stacking faults were observed in the studied nanocrystals and the FFT highlights the WZ nature of the structures.

In the case of the MRs, a detailed TEM analysis of the LAFD samples grown in air can be found in reference [26]. Regarding the MRs produced under a N_2 atmosphere (1 atm), it was verified that the dimensions of the produced MRs were very similar to those grown in air (Figure 11a).
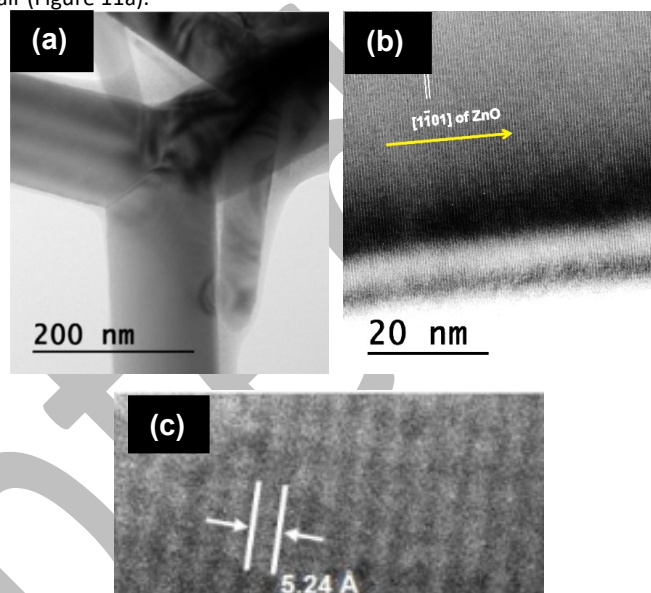
Figure 9 – (a) TEM image of ZnO TPs grown with a laser power of 60 W in air. (b) HRTEM image of a single ZnO TP branch in the [1$\bar{2}$13] zone axis (growth with the same conditions). (c) HRTEM image of part of TP's branch grown along the [0001] direction, showing the measured interplanar spacing.

HRTEM micrographs show that, also in this case, no structural defects were found in the analysed rods (Figure 11b). High crystalline quality was proved by the FFT image acquired from the HRTEM micrographs (Figure 11c). In line with what was reported for the TPs and for the MRs grown in air [26], the interplanar spacing along the main growth direction ([0001]), estimated from the HRTEM image, was found to be ~ 5.2 Å.

4.2. Optical properties

Tetrapods and nanoparticles. Typical photoluminescence (PL) spectra of the NPs and TPs' samples obtained by LAFD are shown in Figure 12a and b, respectively. Whereas the TPs' emission at low temperature (Figure 12b) is always dominated by the donor-bound excitons (D^0X) [56–58] in the ultraviolet (UV) region and almost no visible luminescence is detected under such conditions, for the NPs (Figure 12a), besides the near band edge (NBE) recombination, the broad visible bands were also identified [2,59,60], with the exception of the sample grown with 2 atm of N_2, where practically no visible luminescence was recorded.

The dominant D^0X emission peaked at ~ 3.36 eV is attributed to the overlap of several emitting lines, designated by I lines [2,56,61]. These

transitions have been previously assigned to different impurities like H (I_4), Al (I_6), Ga (I_8) and In (I_9) [56]. In addition, and as reported by Grabowska *et al.* [62], the surface exciton (SX) recombination near ~ 3.366 eV may also be present, as well as the free exciton (FX) transition, usually found at ~ 3.376 eV [2,56].

In the case of the NPs, a close inspection of the NBE region reveals significant changes between the samples grown in different atmospheres.
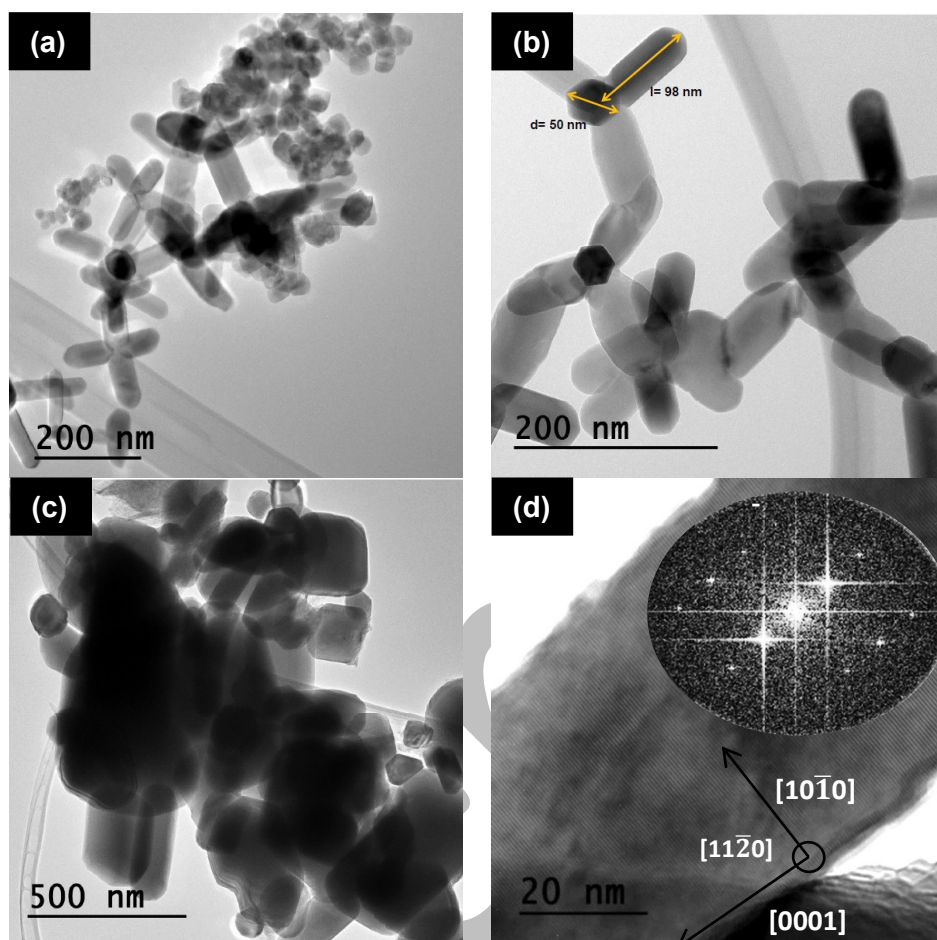
Figure 10 – (a), (b) and (c) TEM images of ZnO samples growth with 35 W under N_2 atmosphere (2 atm). (d) HRTEM image of a selected ZnO TP branch showing its high crystallinity. The inset corresponds to the FFT, pointing to the *c*-axis orientation and WZ crystalline structure.

The NPs grown in air show well-defined NBE transitions, with a narrow D^0X emission and an additional line peaked at ~ 3.31 eV. This line has been widely discussed in the literature and its nature is still under debate. Nevertheless, in a recent work concerning our MRs samples [26], this emission was associated to the presence of surface-related defects. This is also a reproducible feature in all the LAFD NPs, since it was observed in several samples grown in the same conditions, as can be seen in the upper spectra of Figure 12a.

Indeed, for samples grown under the same conditions, the same emission centres are present in the NBE region, however, with a distinct relative intensity regarding the visible broad band. The visible band exhibits a different broadening depending on the analysed sample/sample region. The distinct width of the bands strongly suggests the presence of more than one optically active centre contributing to the broad emission. The different spectral positions can be accounted for different defect distribution. Such broad visible bands are frequently observed in ZnO, either in the bulk, film or nanostructured form. The most common ones are the green (GL) and

yellow luminescence (YL) bands. It is known that different types of defects are responsible for these emissions, but their nature have not been conclusively established yet [2,32,59,63,64].. Both centres appear to be present in the NPs grown by LAFD. In the case of the sample grown with 1 atm of N_2, the broad visible band corresponds to the typically observed unstructured GL. In this case, it is fair to assume an association with oxygen vacancies, since this sample was grown in an oxygen-poor atmosphere. Regarding the NBE of these two samples, a broader emission than that observed for the particles grown in air is observed. In both cases, the emission is peaked at ~ 3.36 eV, likely due to the overlapping of different recombination centres, including the ones identified for the samples grown in air.

The low temperature PL of the ZnO structures is usually used as a reference of the optical quality of the samples, which is generally accounted for a high resolved NBE spectrum, as is the present case both for TPs and NPs grown in air. Another indication of the optical quality of the samples is the ratio between the NBE recombination and the deep level visible emission, which is clearly the case of all the

TPs, where almost no visible emission was detected at low temperature (when compared with the NBE emission), showing their high optical quality.

Microrods. While the TPs emission (Figure 12b) is dominated by the D^{0}X [56–58] and almost no visible luminescence is observed at low temperature, in the case of the MRs (Figure 13), besides the NBE the green broad band is also identified [2,59,60]. Noteworthy, in addition to the FX and D^{0}X lines, the luminescence of these samples is dominated by a line peaked at 3.31 eV, followed by its longitudinal optical (LO) phonon replicas at ∼ 3.24 eV and ∼ 3.16 eV, with an energy separation of ∼ 70 meV. A detailed study on the structural properties and luminescence behaviour in the NBE spectral region for our LAFD ZnO MRs is reported on reference [26] where the ZnO MRs were subjected to post-growth hydrogen and nitrogen plasma treatments. The 3.31 eV emission line was found to be strongly sensitive to these treatments (see inset of Figure 13) and to the excitation density. Despite the still unknown nature of the defects that generate this emission, the performed passivation treatments suggested that surface defects must be considered on the band recombination model [26].

Regarding the GL, the luminescence is centred at ∼ 2.39 eV and exhibits a structured shape with a FWHM close to ∼ 0.43 eV. Although no zero phonon lines were found, the shape of the band resembles a vibronic band with an energy separation between each peak around 72 meV, close to a LO-phonon mode of the ZnO crystal [32]. This structured GL is frequently associated to the presence of Cu impurities, as reported by Dingle and other authors [32,59,60,65].

Even though the GL in the different ZnO structures appear in the same spectral region, the fact that a structureless band is observed for the NPs at low temperature, while a band with a well-defined structure is identified for the MRs, strongly points to the distinct origin of the involved defects [2,59,60,64]. Nevertheless, one should also bear in mind that the shape of the MRs may also play a role in the observation of this structured band since for hexagon-shaped ZnO nanowires, as the present ones, the light can be internally reflected, and, under resonance conditions, strong absorption may occur, given rise to the so-called whispering gallery mode (WGM) resonances [13,66].
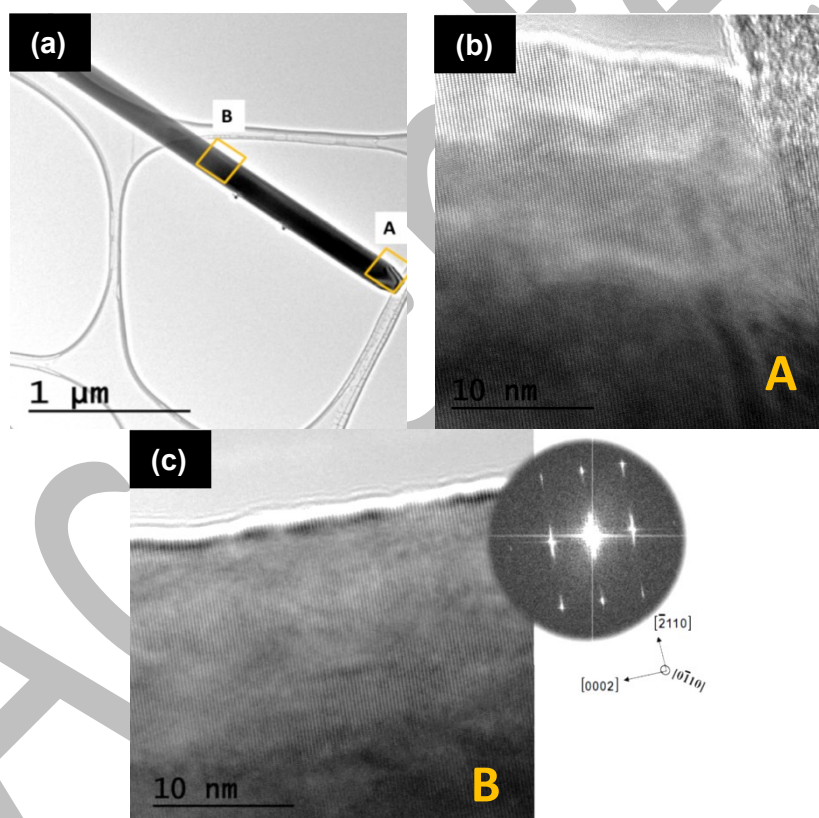
Figure 11 – (a) TEM image of a ZnO rod grown under N$_2$ atmosphere (1 atm). (b) and (c) HRTEM images acquired from the regions marked in (a). The inset corresponds to the FFT confirming *c*-axis orientation and WZ crystalline structure.
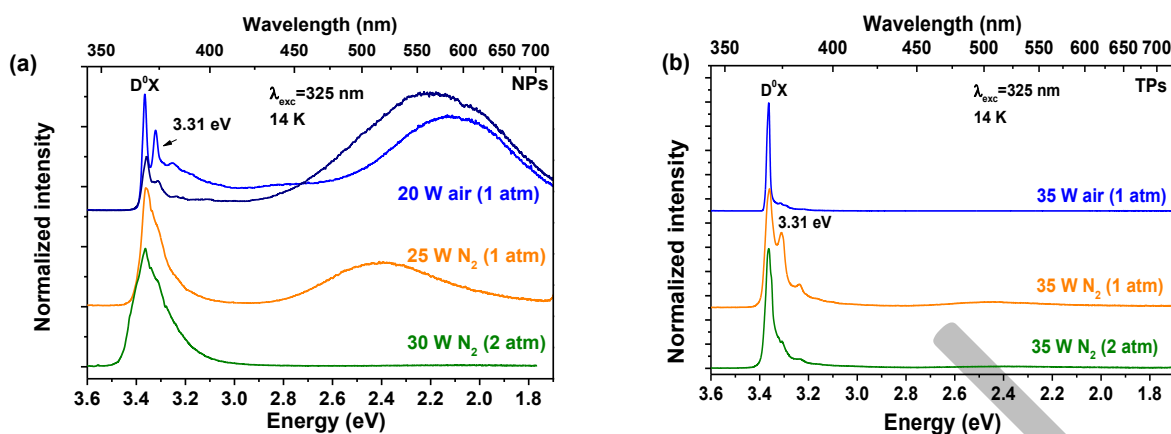
Figure 12 – Low temperature PL spectra of the ZnO (a) NPs and (b) TPs grown under different atmospheres.
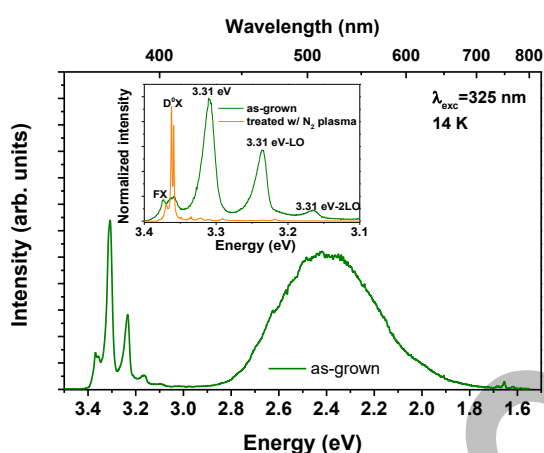

Figure 13 – (a) Low temperature PL spectrum of the ZnO MRs. The inset depicts the high resolution spectra of the NBE emission for the ZnO before and after the treatment with nitrogen plasma.

5. LAFD ZnO-based composites

The potential of ZnO to be employed in some technological applications can be improved by forming complex structures with other materials [67–69]. For instance, the synergetic combination of ZnO with metallic particles [70] has been intensively investigated due to the possibility to modulate their properties [71]. The research on the modification of semiconductors with noble metal ions, as is the case of silver or gold, has gained a significant interest in different technological fields like photocatalysis, sensing, or biomedicine [71–73]. Also carbon-related materials, such as CNTs or graphene, have been widely employed in the formation of composites with ZnO. At the nanoscale, the formation of ZnO-based composites with other materials is expected to alter the properties of both components, giving rise to functional materials with advantageous properties.

The effectiveness of the LAFD method for the growth of such structures was tested in both the ZnO/Ag system [19,21], as well as in ZnO/CNTs samples [19,22,74].

5.1. ZnO grown in the presence of silver.

The production of ZnO/metal nanostructures [68,75] usually involves procedures comprising several steps to produce the desired

materials. LAFD offers the advantage of synthesizing the silver particles directly on the surface of the ZnO MRs or TPs in a single and short step [19,21]. A detailed study on ZnO MRs decorated with silver particles is reported in references [19,21]. It was found that silver was mainly present as small particles attached to the surface of the ZnO structures (Figure 14a and b), with an inhomogeneous distribution (Figure 14c). These droplets tend to accumulate predominantly on the tip of the crystals. It was observed that, especially for the samples grown with powers ≥ 30 W, increasing the nominal Ag concentration, the metal particles assume a catalyst role, promoting the re-nucleation and growth of ZnO crystals on top of the pre-existing ones (Figure 14d).

Even though most of the silver was found on the ZnO surface, XRD measurements suggested an incorporation of some Ag+ ions into the ZnO lattice sites [21]. As reported for the samples without silver [19], increasing the power does not seem to affect significantly the morphology of the crystals, but instead seems to promote the re-nucleation of ZnO in the regions where the silver droplets accumulate. Regarding the optical properties, PL studies performed on the TPs revealed that when the same growth conditions were employed using precursors with and without silver, the resultant samples displayed differences in the energy position of the broad visible bands, as well as in the NBE region [27]. Time-resolved experiments allowed to conclude that the orange-red luminescence detected in the case of the TPs with silver [27] was already present in the samples without this metal and the observed shift in the peak position of the band is due to the suppression of the green component after silver addition. Moreover, in both TPs and MRs, the relative intensity of the surface-related 3.31 eV transition exhibits a decrease. This effect, together with the absence of the GL in the TPs with silver, constitutes an indication of charge transfer from the semiconductor to the metal particles, inhibiting the radiative recombination of the photogenerated electron-hole pairs. The assumption of charge transfer is also corroborated by the reduction of the band tail states in the PL excitation spectra when silver was added (for both morphologies)[27].

5.2. ZnO/CNTs composites

ZnO/CNTs composites have also been produced by the versatile LAFD method, either in the form of ZnO nanostructures deposited on top of vertically aligned CNTs (VACNTs) [22] or nanostructures embedded

in CNTs buckypapers [74]. Different features were observed for these two types of samples. In the first case, ZnO NPs were seen to constitute the first layer (Figure 15a), directly coating the CNTs, while TPs were deposited on top of the NPs' layer, showing no attachment to the CNTs array. PL studies enabled the identification of an enhancement of the overall ZnO emission when deposited on the VACNTs and no changes in the spectral shape were identified [22]. The electrical properties revealed a rectifying behaviour, different from the one obtained for the ZnO sample by itself, while electrical measurements in the VACNTs array showed an ohmic response. For the buckypapers SEM images showed that the TPs were well dispersed (Figure 15b) in the composite, while the NPs presented some agglomerates (Figure 15c). The resistivity was shown to be similar in all samples ($\sim 10^{-1}$ $\Omega \cdot cm$), even when compared to buckypapers prepared only with CNTs, demonstrating that this parameter is ruled by the carbon material with barely no influence from the semiconductor structures. Regarding the PL properties, and in opposition to what happens in the ZnO/VACNTs, in this case slight changes in the shape of the NBE emission were observed for the composites, especially in the case of the sample with TPs. A strong increase in the 3.31 eV line was observed when the TPs were mixed with the CNTs, which was accounted by a higher concentration of electron–hole pairs in the surface of the semiconductor promoted by its contact with the CNTs [74]. The difference observed in the two types of composites can be explained considering that in the latter case the ZnO structures are more dispersed in the CNT buckypaper, having a higher surface area in contact with the carbon material, while in the former, only the first ZnO layer is in direct contact with the VACNTs. The observed combination of ZnO optical and CNTs electrical properties highlights the potential importance of this type of composite materials for technological applications.

6. Prospect applications

The potential of the LADF produced structures was also assessed in different fields, namely in the production of photovoltaic devices and in photocatalysis applications.

6.1 Dye sensitised solar cells

As worldwide energy demand increases, conventional energy resources are expected to reach an end in a near future [76]. In this sense, intensive research has been devoted to find alternatives for energy production. Photovoltaic cells constitute ideal devices, able to provide clean electrical energy (without any other fuel sources or releasing pollutant sub-products to the environment [76,77]. Among the new generation of nanostructured photovoltaic devices, dye-sensitised solar cells (DSSCs) have been subject of an intense research worldwide. This type of solar cells offers low cost and reasonably high light-to-electricity conversion efficiency [78], as well as innovative design opportunities, such as transparency and multicolour options, flexibility and lightweight [79].

The most widely used semiconductor oxide for this type of photovoltaic devices is TiO_2, since it is the one that exhibits the highest efficiencies up to now [80,81]. ZnO is supposed to be a potential substitute for TiO_2 owning to their similar bandgap and electron affinities [82,83], besides its low cost and non-toxicity. It has a great variety of nanostructured morphologies, which is expected to offer a

wide range of photoelectrode architectures/networks, enabling the design of surface areas that maximise the dye adsorption [79,82–85]. TP-like structures have attracted attention due to their unique transport properties, demonstrating higher electron transfer efficiency when compared with a rod morphology and reducing the number of intercrystalline contacts between grain boundaries [86,87]. Additionally, the branching structure is expected to provide a large surface area for sensitisation and charge separation [5,83]. Therefore, a network of the low-dimensional structures (TPs and NPs) produced by LAFD was employed in the production of DSSC devices, as reported in reference [5]. These ZnO structures were used as the active area for the photovoltaic device [5].

The performance of the cell was compared with other ZnO morphologies prepared by different methods (hydrothermal and colloidal synthesis), using the same procedure for the fabrication of the DSSCs and the same area of photoelectrode. The best efficiency was attained for the device where a combination of TPs and NPs produced by the LAFD was used. The formed network revealed a maximum efficiency of 2.9 % for a residence time in a Ru-based dye of 1 h, under simulated air mass (AM) 1.5 illumination conditions.

Further optimisation in the DSSCs fabrication process is still in progress in order to improve device efficiency. Nevertheless, this work proved that LAFD can be a suitable technique to produce high quality ZnO nanostructures to be incorporated in such kind of devices [5].

6.2 Photocatalysis

In the last decades, an increasing interest has been devoted to the research of solutions to treat the wastewaters that are highly contaminated with residual products from several industries, constituting a serious environmental problem [88]. The use of photoactive oxides as catalysts have been subjected to considerable interest, due to their ability to induce the indirect transformations of pollutants into harmless products [89,90].

ZnO is known to possess a very high surface reactivity [91,92], which is beneficial for an efficient visible light photocatalyst [91]. Thus, preliminary studies on the photocatalytic activity of the ZnO TPs and MRs synthesised by LAFD were already carried out, as reported in reference [27]. Furthermore, the mentioned work also assessed the effect of the addition of silver ($\sim$ 3 mol % added to the precursor rods) on the overall photocatalytic response.

The UV photocatalytic activities of ZnO structures grown by LAFD were evaluated at RT from the degradation of methylene blue (MB) as a model dye. As in the work reported by Pimentel *et al.* [7], the photodegradation was found to be dependent on the size and morphology of the structures. A much faster degradation was seen to occur when TPs were used (MB concentration reduced by 50% in $\sim$ 60 minutes) than in the case of the MRs ($\sim$ 150 minutes). Since the photocatalytic reaction occurs at the surface [93,94], it is estimated that structures with nanoscale dimensions, and thus higher surface area, would increase the decomposition rate of the pollutants [94], explaining why a better performance was obtained for the TPs. Their nanometric dimensions lead to a higher surface to volume ratio when compared to the MRs. Moreover, the surface area of the TPs is further increased due to their shape, with high aspect ratio branches and needle-like tips.
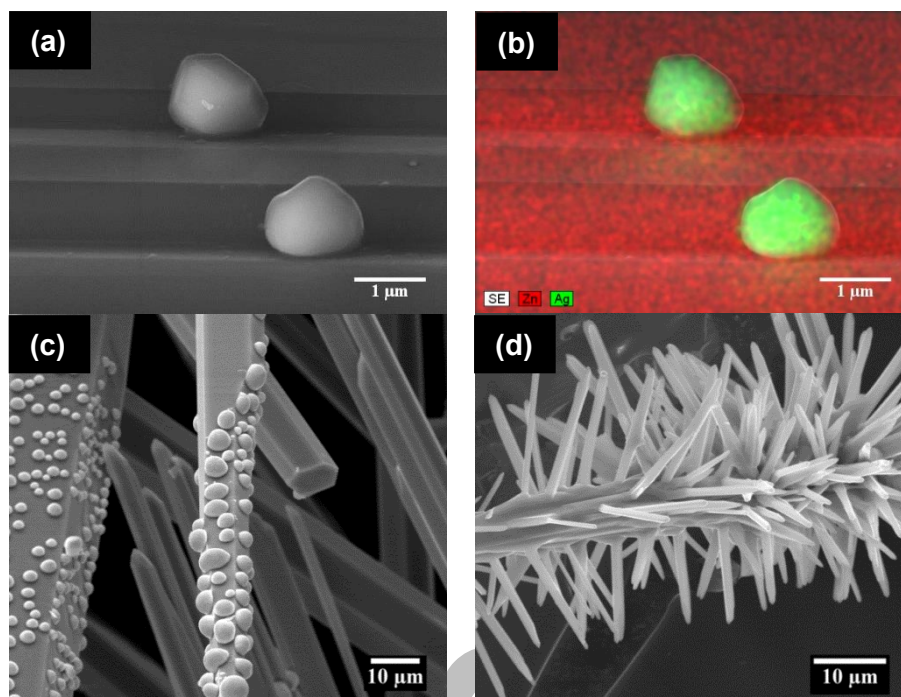
Figure 14 – (a) SEM image of Ag particles on the surface of the ZnO MRs. (b) EDS elemental map of the same region, evidencing that the particles are indeed composed by silver. (c) SEM image of ZnO MRs grown in the presence of silver (1 mol% Ag). (d) SEM image of ZnO MRs grown in the presence of 5 mol% Ag and with 35 W, evidencing the re-nucleation of the ZnO promoted by the presence of Ag.
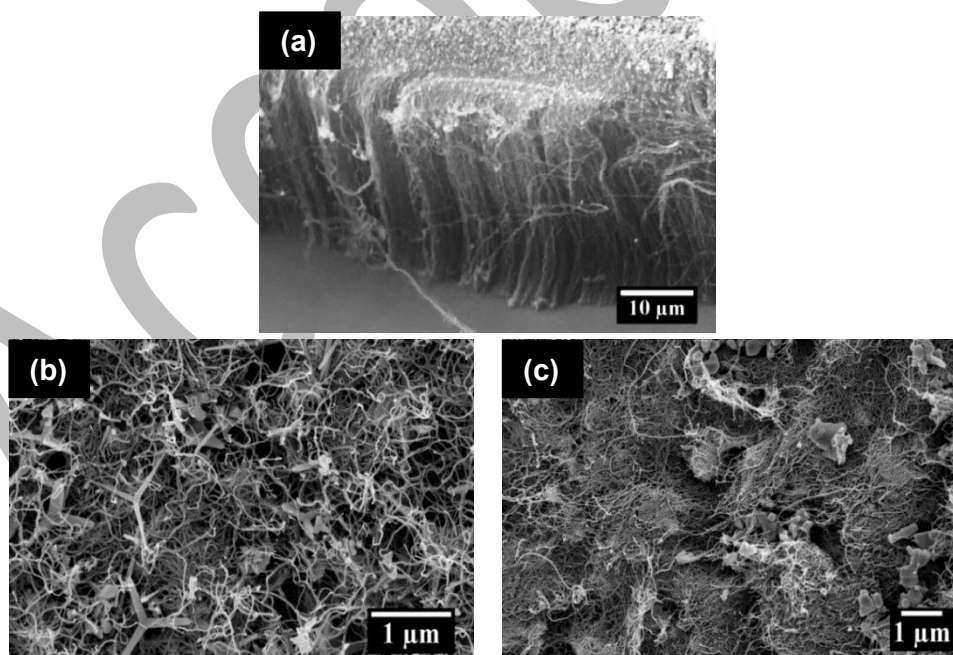
Figure 15 – SEM micrographs of: (a) a cross-section of a ZnO/VACNTs sample prepared by LAFD, showing that the nanoparticles are only deposited on the top of the VACNTs array; (b) CNTs/ZnO TPs buckypaper and (c) CNTs/ZnO NPs buckypaper.

ARTICLE

Such configuration is expected to avoid easy aggregation in solution, which is a problem frequently encountered in NPs, making these networks appealing for such applications [6]. Their shape/size, the low tendency for particle aggregation, together with the highly open and porous network structure formed by the interconnected TPs constitutes an important advantage when a high specific surface area is needed.

The degradation time was further decreased in both structures when silver was added. In the case of the TPs, this time was reduced by more than half and only 24 minutes were necessary to decrease the MB concentration to half of the initial one. For the MRs the decrease was less pronounced, only around 28%, which resulted in a degradation time of $\sim$ 130 minutes. This increase in the photocatalytic activity is likely associated to a more efficient charge separation, promoted by the presence of the metal particles on the surface of the semiconductor. In fact, a reduction of the signal associated with surface-related defects was detected in the PL spectra of the analysed samples, corroborating this hypothesis.

These preliminary results demonstrated the strong size/morphology dependence in the pollutant degradation, as well as the benefits of adding silver to the structures. Since this addition can be accomplished simply by introducing the metal in the precursor rod, a single-step production of ZnO/Ag composites is possible, which is a major advantage for the production of such materials.

7 Other materials grown by LAFD

Besides ZnO, SnO_2 nanostructures were also grown by LAFD, as reported by Santos *et al.* [20]. Undoped and europium-doped (SnO_2:Eu) nanostructures were produced and deposited on silicon substrates. The doping of the structures was accomplished *in-situ* by adding europium oxide to the SnO_2 precursors.

In opposition to what was verified for ZnO, in the case of SnO_2, only nanoparticles were formed independently of the explored growth parameters. In fact, the applied laser power only seemed to affect the amount of deposited material during growth, with a high yield identified for powers above 35 W. The morphology of the SnO_2 and SnO_2:Eu nanocrystals was seen to always be polyhedral [20], with an uniform size distribution of $\sim$ 60 nm, and exhibiting bipyramidal structures, which constitute typical habits of the SnO_2 material [95].

Structural analysis indicated that high crystalline quality nanocrystals were developed under the used growth parameters and no secondary phases were found for the doped samples, proving that the LAFD can be an effective method for material doping. The PL properties of the SnO_2 and SnO_2:Eu nanocrystals were also investigated [20]. For the SnO_2:Eu crystals, the intra-$4f^6$ lines of Eu^{3+} ions were observed overlapped with the broad bands also identified in the undoped samples. The observation of these atomic-like lines corroborates the assumption that the ions are in fact incorporated inside the semiconductor lattice, occupying a well-defined crystalline environment in almost undistorted centrosymmetric sites.

Conclusions

The LAFD method is a suitable technique to grow highly crystalline ZnO micro and nanocrystals, enabling to produce different types of morphologies in the same run of growth, depending on the thermodynamic and kinetic conditions inside the growth chamber. Although several morphologies can be found, the dominant ones include NPs, TPs and MRs. The latter are essentially grown on the top of the precursor rod, while the former are mainly found at a lower temperature region, near the surface of the substrate/holder. The morphologies of the material grown in this region can be controlled by an adequate choice of the growth parameters. The most important ones were found to be the laser power (temperature) and the growth atmosphere (oxygen availability). A self-catalytic VS mechanism was accounted for the nucleation and growth of the nanoscale ZnO structures, while for the MRs a self-catalytic VLS mechanism is proposed. TEM measurements confirmed the high crystallinity of all produced structures and the absence of dislocations or stacking faults, even when poor-oxygen atmospheres were employed. The high crystallinity of the LAFD-grown structures was also corroborated by XRD measurements. Moreover, the optical characterization also put in evidence the high optical quality of these crystals

Advantages of the LAFD growth technique include its catalyst-free nature, being highly versatile to grow ZnO nano/microcrystals at relatively high synthesis rates (depending on the applied laser power), allowing the production of doped and composite materials in a single-step, avoiding time-consuming operations and thus being easily up scalable to large area deposition. Furthermore, this is a simple method that prevents contamination, since no crucibles or supplementary reagents are used. The potential applications of the LADF-produced ZnO structures in the photocatalysis and photovoltaic fields were tested, evidencing promising results.

Finally, this technique was shown to be suitable for the growth of other oxide materials, as is the case of SnO_2, which also evidenced good structural and optical properties, thus, not limiting this technique only to the production of ZnO.

Conflicts of interest

An uncorrected version of this work was temporarily available online without the permission of the authors.

Acknowledgements

Notes and references

1   D. C. Look, *Mater. Sci. Eng. B*, 2001, **80**, 383–387.
2   U. Özgür, Y. I. Alivov, C. Liu, A. Teke, M. A. Reshchikov, S. Doğan, V. Avrutin, S.-J. Cho and H. Morkoç, *J. Appl. Phys.*, 2005, **98**, 041301.
3   D. Wei, H. E. Unalan, D. Han, Q. Zhang, L. Niu, G. Amaratunga and T. Ryhanen, *Nanotechnology*, 2008, **19**, 424006.
4   N. O. V. Plank, I. Howard, A. Rao, M. W. B. Wilson, C. Ducati, R. S. Mane, J. S. Bendall, R. R. M. Louca, N. C. Greenham, H. Miura, R. H. Friend, H. J. Snaith and M. E. Welland, *J. Phys. Chem. C*, 2009, **113**, 18515–18522.
5   J. Rodrigues, A. F. R. Cerqueira, M. G. Sousa, N. F. Santos, A. Pimentel, E. Fortunato, A. F. da Cunha, T. Monteiro and F. M. Costa, *Mater. Chem. Phys.*, 2016, **177**, 322–329.
6   Y. K. Mishra, G. Modi, V. Cretu, V. Postica, O. Lupan, T. Reimer, I. Paulowicz, V. Hrkac, W. Benecke, L. Kienle and R. Adelung, *ACS Appl. Mater. Interfaces*, 2015, **7**, 14303–14316.
7   A. Pimentel, J. Rodrigues, P. Duarte, D. Nunes, F. M. Costa, T. Monteiro, R. Martins and E. Fortunato, *J. Mater. Sci.*, 2015, **50**, 5777–5787.
8   S. S. Bhat, A. Qurashi and F. A. Khanday, *TrAC Trends Anal. Chem.*, 2017, **86**, 1–13.
9   L. Zheng, Y. Wan, P. Qi, Y. Sun, D. Zhang and L. Yu, *Talanta*, 2017, **167**, 600–606.
10   A. Kołodziejczak-Radzimska and T. Jesionowski, *Materials (Basel).*, 2014, **7**, 2833–2881.
11   T. L. Sounart, J. Liu, J. A. Voigt, M. Huo, E. D. Spoerke and B. McKenzie, *J. Am. Chem. Soc.*, 2007, **129**, 15786–15793.
12   G.-C. Yi, C. Wang and W. Il Park, *Semicond. Sci. Technol.*, 2005, **20**, S22–S34.
13   Y. K. Mishra and R. Adelung, *Mater. Today*, 2017, **21**, 631–651.
14   J.-F. Tang, H.-H. Su, Y.-M. Lu and S.-Y. Chu, *CrystEngComm*, 2015, **17**, 592–597.
15   Q. X. Zhao, P. Klason and M. Willander, *Appl. Phys. A*, 2007, **88**, 27–30.
16   G. Dhanaraj, K. Byrappa, V. Prasad and M. Dudley, Eds., *Springer Handbook of Crystal Growth*, Springer, 2010.
17   Z. L. Wang, *J. Phys. Condens. Matter*, 2004, **16**, R829–R858.
18   J. Rodrigues, M. Peres, M. R. N. Soares, A. J. S. Fernandes, N. Ferreira, M. Ferro, A. J. Neves, T. Monteiro and F. M. Costa, *J. Nano Res.*, 2012, **18–19**, 129–137.
19   J. Rodrigues, A. J. S. Fernandes, D. Mata, T. Holz, R. G. Carvalho, R. Fath Allah, T. Ben, D. Gonzalez, R. F. Silva, A. F. da Cunha, M. R. Correia, L. C. Alves, K. Lorenz, A. J. Neves, F. M. Costa and T. Monteiro, in *SPIE OPTO*, eds. F. H. Teherani, D. C. Look and D. J. Rogers, International Society for Optics and Photonics, 2014, p. 89871F.
20   N. Santos, J. Rodrigues, T. Holz, A. Sena, N. Ben Sedrine, A.

Neves, F. Costa and T. Monteiro, *Phys. Chem. Chem. Phys.*, 2015, **17**, 13512–13519.
21   J. Rodrigues, M. R. N. Soares, R. G. Carvalho, A. J. S. Fernandes, M. R. Correia, T. Monteiro and F. M. Costa, *Thin Solid Films*, 2012, **520**, 4717–4721.
22   J. Rodrigues, D. Mata, A. J. S. Fernandes, M. A. Neto, R. F. Silva, T. Monteiro and F. M. Costa, *Acta Mater.*, 2012, **60**, 5143–5150.
23   F. M. Costa, M. F. Carrasco, R. F. Silva and J. M. Vieira, *Laser Floating Zone. Perspectives on Superconductivity Research,* Nova Science Publishers, 2005.
24   F. Ritzert, L. Westfall and L. Center, *NASA Tech. Memo.*
25   S. M. Koohpayeh, D. Fort and J. S. Abell, *Prog. Cryst. Growth Charact. Mater.*, 2008, **54**, 121–137.
26   J. Rodrigues, T. Holz, R. Fath Allah, D. Gonzalez, T. Ben, M. R. Correia, T. Monteiro and F. M. Costa, *Sci. Rep.*, 2015, **5**, 10783.
27   J. Rodrigues, A. Pimentel, E. Fortunato, T. Monteiro and F. M. Costa, *Phys. status solidi*, 2018, 1800155.
28   M. Asadian, *J. Cryst. Process Technol.*, 2013, **03**, 75–80.
29   J. Sohn, W. Hong, S. Lee and J. Ku, *Sci. Rep.*, 2014, **4**, 5680.
30   W.-J. Li, E.-W. Shi, W.-Z. Zhong and Z.-W. Yin, *J. Cryst. Growth*, 1999, **203**, 186–196.
31   P. Hartman and W. G. Perdok, *Acta Crystallogr.*, 1955, **8**, 49–52.
32   C. Jagadish and S. J. Pearton, *Zinc oxide bulk, thin films and nanostructures: processing, properties and applications*, Elsevier, 2006.
33   M. R. Alenezi, A. S. Alshammari, K. D. G. I. Jayawardena, M. J. Beliatis, S. J. Henley and S. R. P. Silva, *J. Phys. Chem. C. Nanomater. Interfaces*, 2013, **117**, 17850–17858.
34   Y. Dai, Y. Zhang and Z. L. Wang, *Solid State Commun.*, 2003, **126**, 629–633.
35   M. Shiojiri and C. Kaito, *J. Cryst. Growth*, 1981, **52**, **Part 1**, 173–177.
36   H. Iwanaga, M. Fujii and S. Takeuchi, *J. Cryst. Growth*, 1993, **134**, 275–280.
37   H. Iwanaga, M. Fujii and S. Takeuchi, *J. Cryst. Growth*, 1998, **183**, 190–195.
38   Y. Ding, Z. L. Wang, T. Sun and J. Qiu, *Appl. Phys. Lett.*, 2007, **90**, 153510.
39   C. Ronning, N. G. Shang, I. Gerhards, H. Hofsäss and M. Seibt, *J. Appl. Phys.*, 2005, **98**, 034307.
40   Z. Chen, Z. Shan, M. S. Cao, L. Lu and S. X. Mao, *Nanotechnology*, 2004, **15**, 365–369.
41   K. Zheng, C. X. Xu, G. P. Zhu, X. Li, J. P. Liu, Y. Yang and X. W. Sun, *Phys. E Low-dimensional Syst. Nanostructures*, 2008, **40**, 2677–2681.
42   Y. Qiu and S. Yang, *Adv. Funct. Mater.*, 2007, **17**, 1345–1352.
43   H. Yan, R. He, J. Pham and P. Yang, *Adv. Mater.*, 2003, **15**, 402–405.
44   J.-S. Lee, M.-I. Kang, S. Kim, M.-S. Lee and Y.-K. Lee, *J. Cryst. Growth*, 2003, **249**, 201–207.
45   Z. Zhang, S. J. Wang, T. Yu and T. Wu, *J. Phys. Chem. C*, 2007, **111**, 17500–17505.
46   C. X. Xu and X. W. Sun, *Jpn. J. Appl. Phys.*, 2003, **42**, 4949–4952.
47   D. Yu, T. Trad, J. T. McLeskey, V. Craciun and C. R. Taylor, *Nanoscale Res. Lett.*, 2010, **5**, 1333–1339.
48   H. J. Fan, R. Scholz, F. M. Kolb and M. Zacharias, *Appl. Phys. Lett.*, 2004, **85**, 4142–4144.
49   W. D. Yu, X. M. Li and X. D. Gao, *Appl. Phys. Lett.*, 2004, **84**,

2658–2660.

50 S. Barth, F. Hernandez-Ramirez, J. D. Holmes and A. Romano-Rodriguez, *Prog. Mater. Sci.*, 2010, **55**, 563–627.

51 Gyu-Chul Yi, *Semiconductor Nanostructures for Optoelectronic Devices: Processing, Characterization and Applications (NanoScience and Technology)*, Springer-Verlag, 2012.

52 R. F. Zhuo, H. T. Feng, J. T. Chen, D. Yan, J. J. Feng, H. J. Li, B. S. Geng, S. Cheng, X. Y. Xu and P. X. Yan, *J. Phys. Chem. C*, 2008, **112**, 11767–11775.

53 A. Wander, F. Schedin, P. Steadman, A. Norris, R. McGrath, T. S. Turner, G. Thornton and N. M. Harrison, *Phys. Rev. Lett.*, 2001, **86**, 3811–3814.

54 H. Landolt, R. Börnstein, H. Fischer, O. Madelung and G. Deuschle, *Landolt-Bornstein: Numerical Data and Functional Relationships in Science and Technology, Volume 17*, Springer Verlag, 1987.

55 T. Yao and S.-K. Hong, Eds., *Oxide and Nitride Semiconductors*, Springer, 2009, vol. 12.

56 B. K. Meyer, H. Alves, D. M. Hofmann, W. Kriegseis, D. Forster, F. Bertram, J. Christen, A. Hoffmann, M. Straßburg, M. Dworzak, U. Haboeck and A. V. Rodina, *Phys. status solidi*, 2004, **241**, 231–260.

57 A. Teke, Ü. Özgür, S. Doğan, X. Gu, H. Morkoç, B. Nemeth, J. Nause and H. Everitt, *Phys. Rev. B*, 2004, **70**, 195207.

58 K. Lischka, A. Waag, H. Mariette, J. Neugebauer, M. R. Wagner, H. W. Kunert, A. G. J. Machatine, A. Hoffmann, P. Niyongabo, J. Malherbe and J. Barnas, *Microelectronics J.*, 2009, **40**, 289–292.

59 R. Dingle, *Phys. Rev. Lett.*, 1969, **23**, 579–581.

60 D. Byrne, F. Herklotz, M. O. Henry and E. McGlynn, *J. Phys. Condens. Matter*, 2012, **24**, 215802.

61 T. Monteiro, A. J. Neves, M. C. Carmo, M. J. Soares, M. Peres, J. Wang, E. Alves, E. Rita and U. Wahl, *J. Appl. Phys.*, 2005, **98**, 013502.

62 J. Grabowska, A. Meaney, K. K. Nanda, J.-P. Mosnier, M. O. Henry, J.-R. Duclère and E. McGlynn, *Phys. Rev. B*, 2005, **71**, 115439.

63 A. B. Djurišić, Y. H. Leung, K. H. Tam, Y. F. Hsu, L. Ding, W. K. Ge, Y. C. Zhong, K. S. Wong, W. K. Chan, H. L. Tam, K. W. Cheah, W. M. Kwok and D. L. Phillips, *Nanotechnology*, 2007, **18**, 095702.

64 A. F. Kohan, G. Ceder, D. Morgan and C. G. Van De Walle, *Phys. Rev. B*, 2000, **61**, 19–27.

65 N. Y. Garces, L. Wang, L. Bai, N. C. Giles, L. E. Halliburton and G. Cantwell, *Appl. Phys. Lett.*, 2002, **81**, 622.

66 T. Nobis, E. M. Kaidashev, A. Rahm, M. Lorenz and M. Grundmann, *Phys. Rev. Lett.*, 2004, **93**, 103903.

67 J. Gröttrup, I. Paulowicz, A. Schuchardt, V. Kaidas, S. Kaps, O. Lupan, R. Adelung and Y. K. Mishra, *Ceram. Int.*, 2016, **42**, 8664–8676.

68 V. Postica, J. Gröttrup, R. Adelung, O. Lupan, A. K. Mishra, N. H. de Leeuw, N. Ababii, J. F. C. Carreira, J. Rodrigues, N. Ben Sedrine, M. R. Correia, T. Monteiro, V. Sontea and Y. K. Mishra, *Adv. Funct. Mater.*, 2017, **27**, 1604676.

69 I. Tiginyanu, L. Ghimpu, J. Gröttrup, V. Postolache, M. Mecklenburg, M. A. Stevens-Kalceff, V. Ursaki, N. Payami, R. Feidenhansl, K. Schulte, R. Adelung and Y. K. Mishra, *Sci. Rep.*, 2016, **6**, 32913.

70 Q. Simon, D. Barreca, D. Bekermann, A. Gasparotto, C. Maccato, E. Comini, V. Gombac, P. Fornasiero, O. I. Lebedev, S. Turner, A. Devi, R. A. Fischer and G. Van Tendeloo, *Int. J. Hydrogen Energy*, 2011, **36**, 15527–15537.

71 Y. Zheng, L. Zheng, Y. Zhan, X. Lin, Q. Zheng and K. Wei, *Inorg. Chem.*, 2007, **46**, 6980–6986.

72 R. Georgekutty, M. K. Seery and S. C. Pillai, *J. Phys. Chem. C*, 2008, **112**, 13563–13570.

73 J. Im, J. Singh, J. W. Soares, D. M. Steeves and J. E. Whitten, *J. Phys. Chem. C*, 2011, **115**, 10518–10523.

74 J. Rodrigues, D. Mata, A. Pimentel, D. Nunes, R. Martins, E. Fortunato, A. J. Neves, T. Monteiro and F. M. Costa, *Mater. Sci. Eng. B*, 2015, **195**, 38–44.

75 Q. Xiang, G. Meng, Y. Zhang, J. Xu, P. Xu, Q. Pan and W. Yu, *Sensors Actuators B Chem.*, 2010, **143**, 635–640.

76 S. M. Sze, *Physics of Semiconductor Devices*, Wiley, 1981.

77 T. Sog, *Nanostructured Materials for Solar Energy Conversion*, Elsevier, 2006.

78 J. Xu, K. Fan, W. Shi, K. Li and T. Peng, *Sol. Energy*, 2014, **101**, 150–159.

79 A. Hagfeldt, G. Boschloo, L. Sun, L. Kloo and H. Pettersson, *Chem. Rev.*, 2010, **110**, 6595–6663.

80 S. Mathew, A. Yella, P. Gao, R. Humphry-Baker, B. F. E. Curchod, N. Ashari-Astani, I. Tavernelli, U. Rothlisberger, M. K. Nazeeruddin and M. Grätzel, *Nat. Chem.*, 2014, **6**, 242–7.

81 A. Yella, H.-W. Lee, H. N. Tsao, C. Yi, A. K. Chandiran, M. K. Nazeeruddin, E. W.-G. Diau, C.-Y. Yeh, S. M. Zakeeruddin and M. Grätzel, *Science*, 2011, **334**, 629–34.

82 C.-P. Lee, C.-Y. Chou, C.-Y. Chen, M.-H. Yeh, L.-Y. Lin, R. Vittal, C.-G. Wu and K.-C. Ho, *J. Power Sources*, 2014, **246**, 1–9.

83 Y. F. Hsu, Y. Y. Xi, C. T. Yip, A. B. Djurišić and W. K. Chan, *J. Appl. Phys.*, 2008, **103**, 083114.

84 A. B. Djurišić, X. Liu and Y. H. Leung, *Phys. status solidi - Rapid Res. Lett.*, 2014, **8**, 123–132.

85 Q. Zhang, C. S. Dandeneau, X. Zhou and G. Cao, *Adv. Mater.*, 2009, **21**, 4087–4108.

86 R. R. Bacsa, J. Dexpert-Ghys, M. Verelst, A. Falqui, B. Machado, W. S. Bacsa, P. Chen, S. M. Zakeeruddin, M. Graetzel and P. Serp, *Adv. Funct. Mater.*, 2009, **19**, 875–886.

87 C.-H. Lee, W.-H. Chiu, K.-M. Lee, W.-H. Yen, H.-F. Lin, W.-F. Hsieh and J.-M. Wu, *Electrochim. Acta*, 2010, **55**, 8422–8429.

88 M. J. Height, S. E. Pratsinis, O. Mekasuwandumrong and P. Praserthdam, *Appl. Catal. B Environ.*, 2006, **63**, 305–312.

89 B. Dindar and S. Içli, *J. Photochem. Photobiol. A Chem.*, 2001, **140**, 263–268.

90 S. Xu and Z. L. Wang, *Nano Res.*, 2011, **4**, 1013–1098.

91 S. Baruah, S. S. Sinha, B. Ghosh, S. K. Pal, A. K. Raychaudhuri and J. Dutta, *J. Appl. Phys.*, 2009, **105**, 074308.

92 R. Ullah and J. Dutta, *J. Hazard. Mater.*, 2008, **156**, 194–200.

93 M. Rezapour and N. Talebian, *Mater. Chem. Phys.*, 2011, **129**, 249–255.

94 F. Lu, W. Cai and Y. Zhang, *Adv. Funct. Mater.*, 2008, **18**, 1047–1056.

95 H. W. Kim, S. H. Shim and C. Lee, *Ceram. Int.*, 2006, **32**, 943–946.